



Unspecific peroxygenases immobilized on Pd-loaded three-dimensional ordered macroporous (3DOM) titania photocatalyst for photo-enzyme integrated catalysis

Xuewu Deng^{a,1}, Xiaobing Zheng^{a,1}, Feifei Jia^a, Cuiyao Cao^a, Haolei Song^b, Yanjun Jiang^a, Yunting Liu^a, Guanhua Liu^{a,*}, Shijie Li^{c,*}, Lihui Wang^{a,d,**}

^a School of Chemical Engineering and Technology, Hebei University of Technology, Tianjin 300401, China

^b Hebei Yanuo Bioscience Company Limited by Shares, 19 Alishan Street, Economic and Technological Development Zone, Shijiazhuang 052165, Hebei Province, China

^c National Engineering Research Center for Marine Aquaculture, Zhejiang Ocean University, Zhoushan, Zhejiang Province 316022, China

^d Department of Biochemical Engineering, Tianjin Modern Vocational Technology College, No. 3 Yaguan Road, Jinnan District, Tianjin 300350, China

ARTICLE INFO

Keywords:

Photo-enzyme integrated catalyst
3DOM
TiO₂
Enzyme immobilization
Chiral synthesis

ABSTRACT

The selective oxyfunctionalization of C-H and C=C bonds is highly important and catalyzed by unspecific peroxygenases (UPOs) which suffer from inactivation by hydrogen peroxide (H₂O₂). Herein, photo-enzyme integrated catalysts were constructed by immobilizing AaeUPO as cross-linked enzyme aggregates (CLEAs) in Pd-loaded three-dimensional ordered macroporous titania (3DOM TiO₂) with in situ photocatalytic H₂O₂ production. The prepared AaeUPO@3DOM TiO₂-Pd obtained higher catalytic efficiency compared with CLEAs-AaeUPO. The conversion of ethylbenzene to (*R*)-1-phenethyl alcohol was significantly improved, reaching 99 % compared with free enzyme (38 %) and CLEAs-AaeUPO (49 %), with *ee* value of > 99 %. AaeUPO@3DOM TiO₂-Pd exhibited good stability and reusability attributed to the protection of macropores and in situ H₂O₂ production. By using the designed 3DOM platform for photocatalysis and enzyme immobilization, the in situ photocatalytic generation of H₂O₂ was highly efficient, and the monodisperse CLEAs-AaeUPO in the macropores facilitated the contact of substrate and enzyme, thus obtaining excellent photo-enzyme coupled catalysis.

1. Introduction

The selective oxyfunctionalization of (non-)activated C-H bonds is of great significance while hard to fulfill due to the thermodynamical stability and rather inertness. Chemical synthesis is currently used for this purpose, but the reaction efficiency is generally not satisfactory ascribed to the poor selectivity and unfriendliness to the environment. Biocatalysis has great potential, especially considering the mild condition, high efficiency and high selectivity [1,2]. Unspecific peroxygenases (UPOs, E.C. 1.11.2.1) are promising in catalyzing various oxidation reactions for selective oxyfunctionalization of non-activating C-H and C=C bonds, which can use H₂O₂ as a co-substrate [3]. Particularly, *Agroclybe aegerita* UPO (AaeUPO) from the recombinant fermentation in *Pichia pastoris* can catalyze the hydroxylation, epoxidation, and dealkylation of aliphatic and aromatic compounds [4]. The superiorities

of AaeUPO as an efficient biocatalyst for mono-oxygenation reaction are simple electron transfer process, high catalytic activity, and broad substrate spectrum. Notably, AaeUPO directly utilizes hydrogen peroxide (H₂O₂) to regenerate catalytically active heme, and doesn't rely on a complex and sensitive electron transport chain and an expensive coenzyme (NAD(P)H) compared to P450 with similar catalytic performance. Therefore, AaeUPO is considered an ideal biocatalyst for selectively activating C-H bonds or C=C bonds. While, the application of free AaeUPO is often hindered by their easy inactivation under the condition of adding high concentrated H₂O₂, and poor thermal and pH stability [4, 5]. What's more, free enzyme cannot be recovered from the reaction system, which increases the cost and difficulty of product separation [6]. Overcoming these shortcomings is the key to promoting the large-scale application of AaeUPO.

In order to alleviate the issue that AaeUPO (and even all blood

* Corresponding authors.

** Corresponding author at: School of Chemical Engineering and Technology, Hebei University of Technology, Tianjin 300401, China.

E-mail addresses: gqliu@hebut.edu.cn (G. Liu), lishijie@zjou.edu.cn (S. Li), wanglihui2008@126.com (L. Wang).

¹ These authors contributed equally.

oxygen-dependent enzymes) is irreversibly inactivated in high concentrations of H_2O_2 , a range of in situ H_2O_2 generation systems have been developed, [7] such as chemical, [8] enzymatic, [9] electrochemical, [10] and photocatalytic approaches [11]. Among these methods, photocatalysis can not only degrade pollutants, [12–21] but also utilize light energy to drive the reduction of O_2 to H_2O_2 by simple sacrificial electron donors [22,23]. Various semiconductor-based solid photocatalysts (such as TiO_2 , C_3N_4 , etc.) have been added to free enzyme systems to construct heterogeneous systems, which show high photocatalyst reusability [3]. Nonetheless, the enzymes and photocatalysts generally exist in free form in the reported photo-enzyme-coupled systems, which leads to a long diffusion distance of intermediates and a low use efficiency of the two modules [24]. Another problem is that *AaeUPO* still exists in the form of free enzyme, which cannot realize the recovery and reuse of the expensive enzymes and increases the difficulty for the separation and purification of products in the later stage. Therefore, it is necessary but still challenging to construct photo-enzyme integrated catalyst reasonably [25]. On the one hand, it is necessary to prepare suitable photocatalytic carrier with high photocatalytic reactivity, on the other hand, it is necessary to propose good strategies to make the immobilized enzyme work efficiently and reduce the mass transfer resistance in cascade reaction meanwhile effective recovering the expensive enzyme. How to combine the two processes and develop efficient reactors like chloroplasts that can solely use sunlight to drive the transformation of substance is a problem that researchers have been looking forward to solving [24,26–28].

Converting enzymes from a soluble and unstable catalyst to a heterogeneous and stable catalyst through the binding interaction of enzyme molecule to carrier or among enzyme molecules, immobilized enzyme technology is believed to be the most effective method to enhance enzyme stability and achieve reuses together with easy separation of catalyst and product [6,29–31]. Semiconductor materials could be applied as a carrier to construct immobilized *AaeUPO*, which not only separate the enzyme molecules from the solution, but also generate H_2O_2 in situ [32,33]. Besides, photo-enzyme integrated catalyst can improve catalytic performance and complete reactions that cannot be carried out by a single catalyst through the transfer of reaction substrates between adjacent active sites.

Cross-linked enzyme aggregates (CLEAs) are a promising technology for carrier-free immobilization, which prevents the active sites of enzyme molecules from being decomposed and preserves the enzyme activity to the greatest extent [34]. However, there are also some disadvantages such as lack of particle size control, difficult mass transfer and only partial recovery during centrifugation [35,36]. In order to overcome these problems, the CLEAs were immobilized in a three-dimensional ordered macroporous (3DOM) structure, which can effectively prevent the formation of large particles of CLEAs, and the ordered pores can improve the contact between substrates and enzymes. At the same time, the stability of CLEAs in the reaction environment can be improved, and the CLEAs formed in the large pores make it difficult for the enzyme to filter out thus increasing the enzyme loading.

In this study, a multifunctional 3DOM photocatalyst-assisted carrier, which can generate H_2O_2 in situ under photocatalytic conditions, was constructed to immobilize *AaeUPO* CLEAs. This integrated catalyst coupled with photocatalysis and enzyme catalysis, which improved *AaeUPO* stability and achieved multiple reuses. Then we chose the hydroxylation of ethylbenzene into (*R*)-1-phenethyl alcohol as a model reaction. The integrated catalyst offers *AaeUPO* with high catalytic efficiency, good thermal stability, acid-base resistance and mechanical stability, and the conversion rate in the production of (*R*)-1-phenethyl alcohol was significantly improved thus increasing the application prospect of *AaeUPO* for selective oxyfunctionalization of non-activating C-H and C=C bonds.

2. Experimental section

2.1. Materials

Tetrabutyl titanate (TBOT) and styrene (99 %) were purchased from Kermel. 2,2-azino-bis(3-ethylbenzothiazoline-6-sulfonic acid (ABTS) was purchased from Aladdin (809 Chuhua Branch Road, Fengxian District, Shanghai, China). Sodium hydroxide (NaOH), polyvinyl pyrrolidone (PVP), dipotassium hydrogen phosphate, potassium dihydrogen phosphate, sodium citrate, citric acid and concentrated hydrochloric acid (HCl, 36 wt%) were purchased from Tianjin Chemical Reagent Company (Xiqing District, Tianjin, China). Potassium persulfate ($\text{K}_2\text{S}_2\text{O}_8$), glutaric dialdehyde (GA, 50 %), bovine serum albumin (BSA), and ammonium sulfate ($(\text{NH}_4)_2\text{SO}_4$) were purchased from Macklin (169 Chugong Road, Fengxian District, Shanghai, China). All chemicals and reagents are used without further purification. *AaeUPO* was fermented in our lab.

2.2. Preparation of photocatalysts

2.2.1. Preparation of PS colloidal template

Emulsion polymerization was used to prepare polystyrene (PS) microspheres. 30 g of styrene was washed five times with 2 M NaOH to remove the polymerization inhibitor. 1.2 g PVP and 240 mL water were carefully mixed in a 500 mL round-bottom flask followed by bubbling nitrogen to remove oxygen in the flask and solution. Then the solution was heated to 80 °C in a water bath under nitrogen environment, and the polymerization process was triggered by introducing the initiator $\text{K}_2\text{S}_2\text{O}_8$ (0.4 g). After 24 h of stirring, the process was terminated and the flask was cooled. The PS colloidal template was centrifuged at 3500 rpm and the supernatant was removed.

2.2.2. Preparation of 3DOM TiO_2 -Pd

The precursor solution was prepared by mixing 3 mL concentrated HCl with 4 mL water in 10 mL anhydrous ethanol, followed by adding 10 mL tetrabutyl titanate solution and stirring for 5 min. Under vacuum, the precursor solution was mixed with the PS colloidal template maintained for 12 h. In a tubular furnace, 3DOM TiO_2 was obtained by air calcination at 450 °C for 3 h at a heating rate of 1 °C/min. Then 80 mg 3DOM TiO_2 was mixed with a certain concentration of palladium (Pd) chloride solution followed by adding 1.5 mL sodium borohydride (1 mM) solution to reduce the metal Pd and kept for 1 h. The precipitate was washed three times with water and ethanol, and dried for 8 h at 50 °C in the oven to obtain 3DOM TiO_2 -Pd.

2.2.3. Preparation of *AaeUPO*@3DOM TiO_2 -Pd

25 mg 3DOM TiO_2 -Pd was mixed with 200 μL *AaeUPO* enzyme solution (fermented from *Pichia pastoris*) and a small amount of bovine serum albumin. 4 mL cold saturated $(\text{NH}_4)_2\text{SO}_4$ was added as a precipitant to precipitate for 1 h, and then a certain amount of glutaraldehyde (GA) (25 %) was added as a crosslinking agent, followed by centrifugal washing to obtain coupling catalyst *AaeUPO*@3DOM TiO_2 -Pd.

2.3. Activity evaluation

2.3.1. Performance test of H_2O_2 by photocatalysts

The operating conditions of the photocatalytic reaction were as follows: 50 mg photocatalyst, 10 mL phosphate buffer (pH = 6, 60 mM), 32 mM MeOH, ultrasonic treatment (10 min), Xe lamp (300 W, white light bulb). The generated H_2O_2 can oxidize the divalent iron ions in FOX (Ferrous Oxidation in Xylenol orange) solution and combine with xylenol orange to change from yellow to purple. The concentration of H_2O_2 was detected by UV-visible spectrophotometer at 585 nm. The H_2O_2 formation rate (mM h^{-1}) was calculated according to Eq. (S1).

2.3.2. Photoenzymatic hydroxylation reaction by AaeUPO@3DOM TiO₂-Pd

The reaction solution was composed of 5 g/L catalyst, 15 mM substrate, and 32 mM methanol (MeOH) in phosphate buffer (PBS, pH = 6, 60 mM, 10 mL) at 25 °C for 12 h under simulated sunlight. Error estimates were calculated by at least three replicates.

3. Results and discussion

3.1. Catalyst preparation and characterization

The fabrication scheme of AaeUPO@3DOM TiO₂-Pd is shown in Fig. 1a. First of all, uniform PS colloidal microspheres were synthesized by hydrothermal method. The monodisperse PS microspheres were self-assembled into closely packed photonic crystals by prolonged centrifugation. Afterwards, titanium precursor was penetrated into the PS template followed by hydrolyzing in the interspace. After calcination in air, 3DOM TiO₂ was gained. Finally, 3DOM TiO₂-Pd was obtained after loading Pd. Fig. 1b showed that PS microspheres, with a diameter of about 200 nm, were self-assembled to an opal structure with uniform and orderly arrangement. The 3DOM TiO₂ retained the integrity of the inverse opal structure with a regular structure and developed framework, as shown in Fig. 1c. After Pd loading, the obtained 3DOM TiO₂-Pd (Fig. 1d) maintained an interconnected ordered macroporous structure throughout the catalyst, which could facilitate light capture and enzyme immobilization, and the presence of Pd cannot be seen due to the small size [37,38]. The HR-TEM image (Fig. 1e) revealed the high crystallinity of TiO₂ with lattice spacing of 0.35 nm corresponding to the anatase (101) plane. And Pd nanoparticles (NPs) attached on the TiO₂ surface exhibited lattice spacing of 0.23 nm assigned to FCC(111) crystal faces

of Pd NPs. TEM characterization provided an important basis for the construction of heterostructures. Further EDS mapping (Fig. 1f, g) proved the successful loading of Pd, and the uniform distribution of Ti and Pd, which can effectively improve the effect of heterojunction for photocatalytic ability.

The XRD patterns of 3DOM TiO₂ and 3DOM TiO₂-Pd with different Pd loadings are shown in Fig. 2a. 3DOM-TiO₂ and 3DOM TiO₂-Pd mainly presented in the anatase phase with high crystallization degree, and the 2θ of 25.4 °, 37.9 °, 48.1 °, 53.9 °, 55.2 °, 62.8 ° and 75.1 ° were corresponded to (101), (004), (200), (105), (211), (204) and (215) diffractions (JCPDS No.12-1272) [39–41]. Moreover, two weak diffraction peaks around 27.4 ° and 36.1 ° also appeared, corresponding to the (110) and (101) planes of the rutile phase. Thus the 3DOM TiO₂ support was mainly anatase TiO₂ [38]. No diffraction peaks of Pd NPs could be observed due to the low loading and small size. The Raman spectra in Fig. 2b showed peaks at 144 cm⁻¹ (Eg), 397 cm⁻¹ (B1g), 517 cm⁻¹ (A1g), and 640 cm⁻¹ (Eg), which were the characteristics of the anatase TiO₂ phase. The peak at 144 cm⁻¹ was ascribed to the bending vibration of O–Ti–O bond, and the other three peaks were assigned to Ti–O–Ti bending. The Raman spectra demonstrated the presence of two crystal phases as indicated by the XRD patterns. The Raman spectrum did not change after the loading of the Pd NPs on TiO₂.

The optical absorption properties and energy band gaps of 3DOM TiO₂ and 3DOM TiO₂-Pd with different Pd loadings were investigated by UV-Vis absorption spectroscopy [42]. Fig. 3a showed that the maximum absorption wavelengths of 3DOM TiO₂ and 3DOM TiO₂-Pd with Pd loadings of 0.25 %, 0.5 %, 0.75 %, and 1.25 % were located at 413 nm, 421 nm, 423 nm, 424 nm and 425 nm, respectively. The absorption edge of 3DOM TiO₂ loaded with Pd manifested a significant red shift in comparison to pure 3DOM TiO₂, demonstrating that the loading of Pd

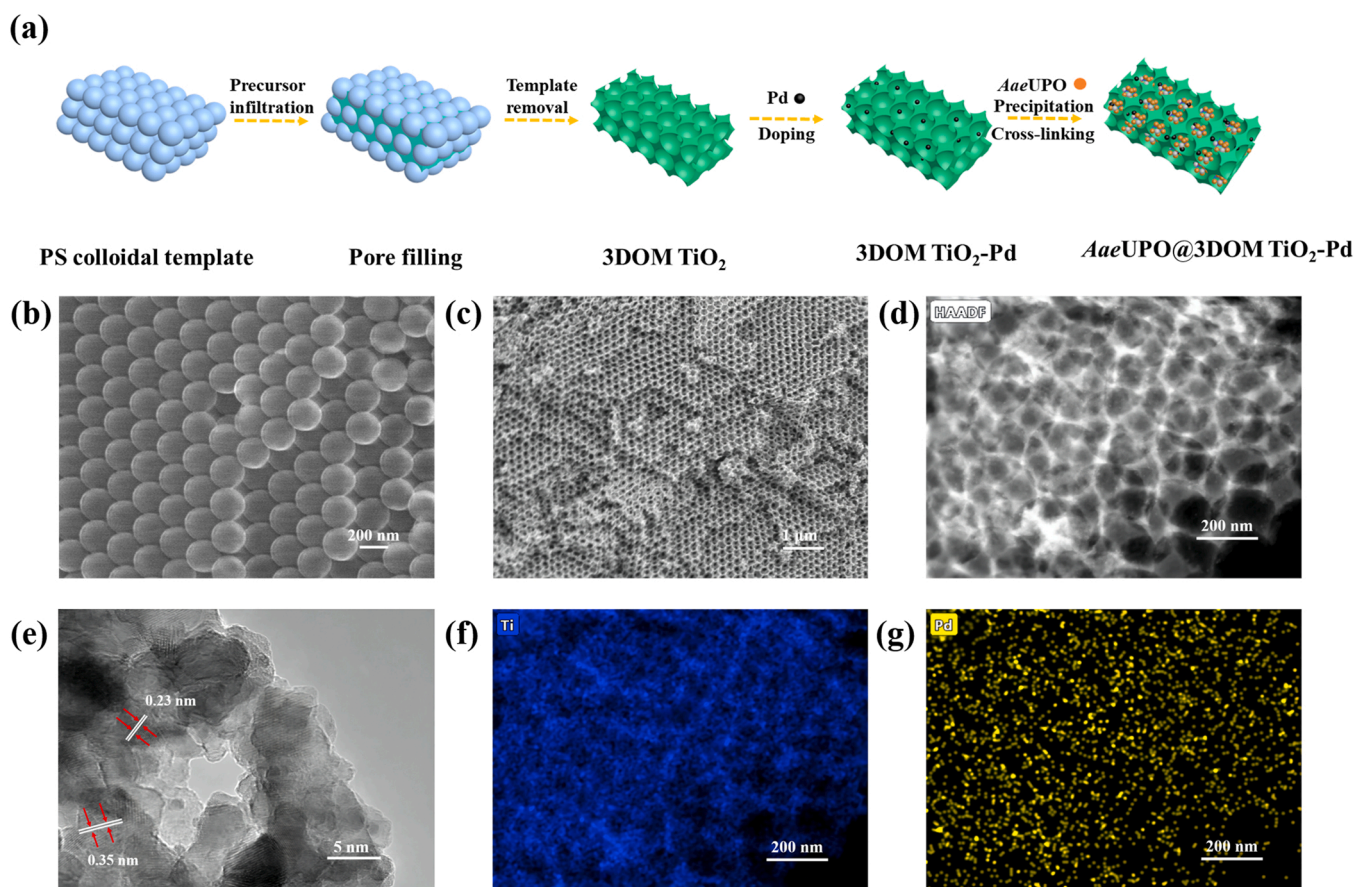


Fig. 1. Schematic diagram of AaeUPO@3DOM TiO₂-Pd preparation (a); SEM images of PS microspheres (b) and 3DOM TiO₂ (c); TEM image (d), HR-TEM image (e), and element mapping (f, g) of 3DOM TiO₂-Pd.

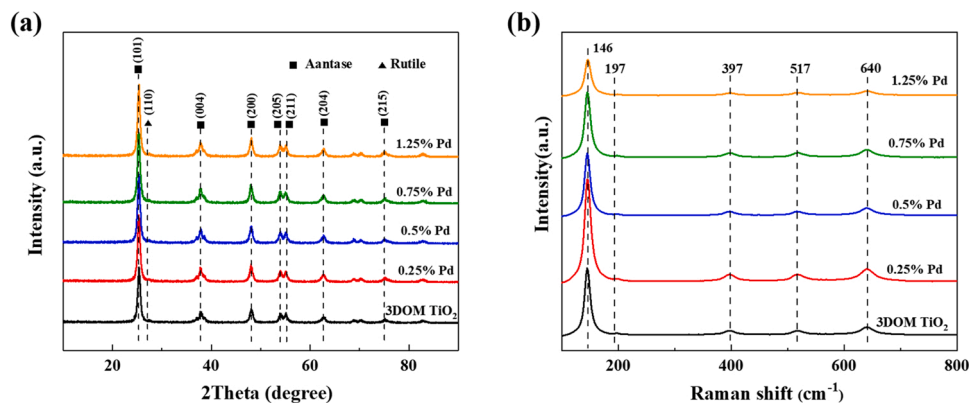


Fig. 2. XRD patterns (a), Raman spectra (b) of 3DOM TiO₂ and 3DOM TiO₂-Pd with different Pd additive content.

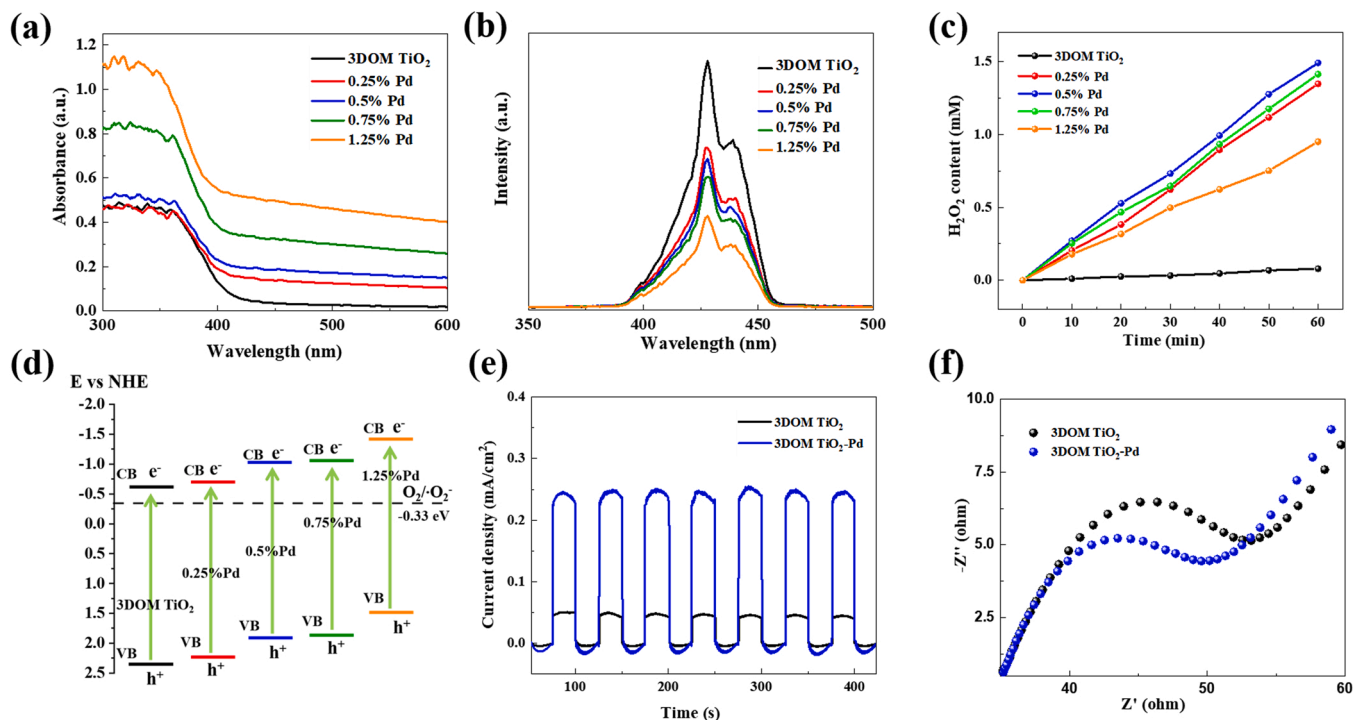


Fig. 3. UV-vis spectra (a); PL spectra (b); H₂O₂ formation rate of 3DOM TiO₂ and 3DOM TiO₂-Pd with different Pd additive content (c); band alignment (d); photocurrent density (e) (under 300 W Xe lamp irradiation in a 0.5 mol/L Na₂SO₄ solution); EIS Nyquist plots (f).

could extend the range of light response [43]. The energy bands of 3DOM TiO₂ and 3DOM TiO₂-Pd with Pd loadings of 0.25 %, 0.5 %, 0.75 %, and 1.25 % were estimated by K-M transformation (Fig. S1) to be 3.01 eV, 2.95 eV, 2.94 eV, 2.91 eV, 2.89 eV, respectively. The band value gradually decreased with the increase of Pd loading, which was due to the property of Pd as an electron acceptor [44–46]. The valence band (VB) values of 3DOM TiO₂, 3DOM TiO₂-Pd with Pd loadings of 0.25 %, 0.5 %, 0.75 %, and 1.25 % are 2.38 eV, 2.24 eV, 1.91 eV, 1.86 eV and 1.49 eV, respectively, calculated by VB XPS (Fig. S2). The conduction band (CB) positions of 3DOM TiO₂-Pd and 3DOM TiO₂ were calculated according to the band gap and VB position. As shown in Fig. 3d, the CB potentials of 3DOM TiO₂, 3DOM TiO₂-Pd with Pd loadings of 0.25 %, 0.5 %, 0.75 %, and 1.25 % are −0.63 eV, −0.71 eV, −1.03 eV, −1.05 eV and −1.40 eV, respectively. The CB position of 3DOM TiO₂-Pd was more negative than 3DOM TiO₂ and the potential for oxygen reduction. Therefore, 3DOM TiO₂-Pd had a stronger reducing ability, so the photogenerated electrons on the CB activated oxygen to generate superoxide anion radical ([•]O₂[−]). Besides, the doping of Pd NPs

markedly enhanced the spatial separation of electrons and holes, as verified by the steady-state photoluminescence (PL) emission spectra [47,48]. As shown in Fig. 3b, all samples showed strong fluorescence signals at 430–450 nm, which was attributed to the process of electrons returning from the excited state to the ground state. The fluorescence intensity of 3DOM TiO₂ was the highest, and the intensity decreased greatly after loading with Pd, which indicated that the recombination of photogenerated charges was suppressed to a large extent.

In most photo-enzyme-coupled systems, enzymes with free state caused long diffusion distances for intermediates and inefficient utilization of enzyme modules [49]. Herein, enzyme was immobilized on the photocatalyst to construct an integrated catalyst. In addition, the heme protein structure of the active center of AaeUPO is easily destroyed by high concentrations of H₂O₂, [32] so photocatalysts were used to generate H₂O₂ in situ to avoid the rapid deactivation of enzyme. Fig. 3c shows the H₂O₂ production capacity of 3DOM TiO₂ with different Pd loadings. The produced H₂O₂ content in the pristine 3DOM TiO₂ solution was very low (~0.08 mM h^{−1}), and the H₂O₂ content was

significantly increased after loading Pd. H_2O_2 production reached a maximum of $1.49 \text{ mM}\cdot\text{h}^{-1}$ (18.9 times compared with pure 3DOM TiO_2) when the loading concentration of Pd was 0.5 %. The photo-excited electrons in the CB of 3DOM TiO_2 can be transferred to metal Pd. Electrons are trapped in Pd due to the formation of the Schottky barrier which increased the lifetime of electron-hole pairs and boosted the photoreactivity. When the adding amount of Pd in 3DOM TiO_2 further increased to 1.25 %, the concentration of H_2O_2 decreased. On the one hand, the catalyst that generates H_2O_2 was also active for the decomposition of H_2O_2 [50]. On the other hand, when the palladium loading reached 1.25 %, the palladium agglomeration phenomenon was obvious (Fig. S3). These were not conducive to H_2O_2 production. Appropriate amount of Pd that supported on the surface of 3DOM TiO_2 can effectively facilitate the generation of H_2O_2 from O_2 [50]. We tested the H_2O_2 production capacity of $\text{AaeUPO}@3\text{DOM TiO}_2\text{-Pd}$. The results (Fig. S4) showed that the protein loading had little effect on the H_2O_2 production capacity of the photocatalyst. Finally, 3DOM $\text{TiO}_2\text{-Pd}$ with Pd adding amount of 0.5 % was selected for enzyme immobilization. Therefore 0.5 % was the default additive content of Pd in the following experiments.

To further demonstrate the improvement in separation efficiency of photogenerated electrons and holes by Pd NPs, we conducted photoelectrochemical experiments including transient photocurrent and electrochemical impedance spectroscopy (EIS). Both 3DOM TiO_2 and 3DOM $\text{TiO}_2\text{-Pd}$ exhibited sensitive on-off photocurrent responses. As shown in Fig. 3e, the photocurrent density of the 3DOM $\text{TiO}_2\text{-Pd}$ is 5 times of 3DOM TiO_2 , demonstrating that the photoinduced electrons prefer to separate and transfer to surface fast after the loading of Pd. The diameter of semicircle of the arch in the Nyquist plot reflects charge transfer resistance. The samples with Pd NPs (3DOM $\text{TiO}_2\text{-Pd}$) showed smaller semicircle than 3DOM TiO_2 (Fig. 3f), indicating the doping of Pd NPs remarkably improved the separation of photogenerated electrons and holes.

The FTIR spectra (Fig. 4a) of 3DOM TiO_2 , 3DOM $\text{TiO}_2\text{-Pd}$ and $\text{AaeUPO}@3\text{DOM TiO}_2\text{-Pd}$ all observed an absorption peak at 477 cm^{-1}

correlating to the Ti–O–Ti bond in TiO_2 . Compared with 3DOM TiO_2 and 3DOM $\text{TiO}_2\text{-Pd}$, both free AaeUPO and $\text{AaeUPO}@3\text{DOM TiO}_2\text{-Pd}$ observed an absorption peak located at 3250 cm^{-1} corresponding to the N–H stretching vibration, and at 1100 cm^{-1} and 1400 cm^{-1} corresponding to the C–N stretching vibration. Compared with 3DOM TiO_2 and 3DOM $\text{TiO}_2\text{-Pd}$, the enhanced peaks at 1100 cm^{-1} and 1400 cm^{-1} for free AaeUPO and $\text{AaeUPO}@3\text{DOM TiO}_2\text{-Pd}$ indicated that new C–N bonds were generated during the crosslinking process [34,51,52]. These results demonstrated that AaeUPO was successfully immobilized on the 3DOM $\text{TiO}_2\text{-Pd}$ carrier. As shown in the SEM image of $\text{AaeUPO}@3\text{DOM TiO}_2\text{-Pd}$ (Fig. 4b), the macroporous channels were filled with CLEAs of AaeUPO obtaining monodisperse CLEAs by the rigid compartment of 3DOM $\text{TiO}_2\text{-Pd}$ photocatalyst. As shown in Fig. 4c, the AaeUPO molecules labeled with rhodamine B were immobilized in 3DOM $\text{TiO}_2\text{-Pd}$, and the fluorescence was detected. The red fluorescence emitted by the labeled enzyme molecule was displayed in the whole area, which proved that the enzyme was successfully immobilized.

To further study the composition and chemical states of 3DOM TiO_2 , 3DOM $\text{TiO}_2\text{-Pd}$ and $\text{AaeUPO}@3\text{DOM TiO}_2\text{-Pd}$, we performed surface X-ray photoelectron spectroscopy (XPS). As shown in Fig. 4d, the increase in the intensity of N indicates that the enzyme has been successfully immobilized on the support. Fig. 4e presented two bands with binding energies of 458.2 eV and 463.7 eV corresponding to $\text{Ti } 2p_{3/2}$ and $\text{Ti } 2p_{1/2}$, respectively from Ti^{4+} in pure 3DOM TiO_2 . Compared with 3DOM TiO_2 (458.1 eV), a red shift of 0.1 eV to lower binding energy in the peak positions of 3DOM $\text{TiO}_2\text{-Pd}$ and $\text{AaeUPO}@3\text{DOM TiO}_2\text{-Pd}$ (458.2 eV) was observed, illustrating that the charge transfer between Pd NPs and 3DOM TiO_2 probably occurred. Fig. 4f showed the Pd 3d high-resolution spectrum of the 3DOM $\text{TiO}_2\text{-Pd}$, which was split into four peaks at 334.8, 336, 340, and 343 eV. The peaks at 334.8 and 340 eV belonged to metallic Pd^0 states of $\text{Pd } 3d_{3/2}$ and $\text{Pd } 3d_{5/2}$, respectively. The peaks of $\text{Pd } 3d_{3/2}$ and $\text{Pd } 3d_{5/2}$ located at 343 and 336 eV correspond to Pd^{2+} bound to oxygen, respectively. These results confirm the coexistence of metallic Pd^0 and oxidized Pd^{2+} in 3DOM $\text{TiO}_2\text{-Pd}$ samples.

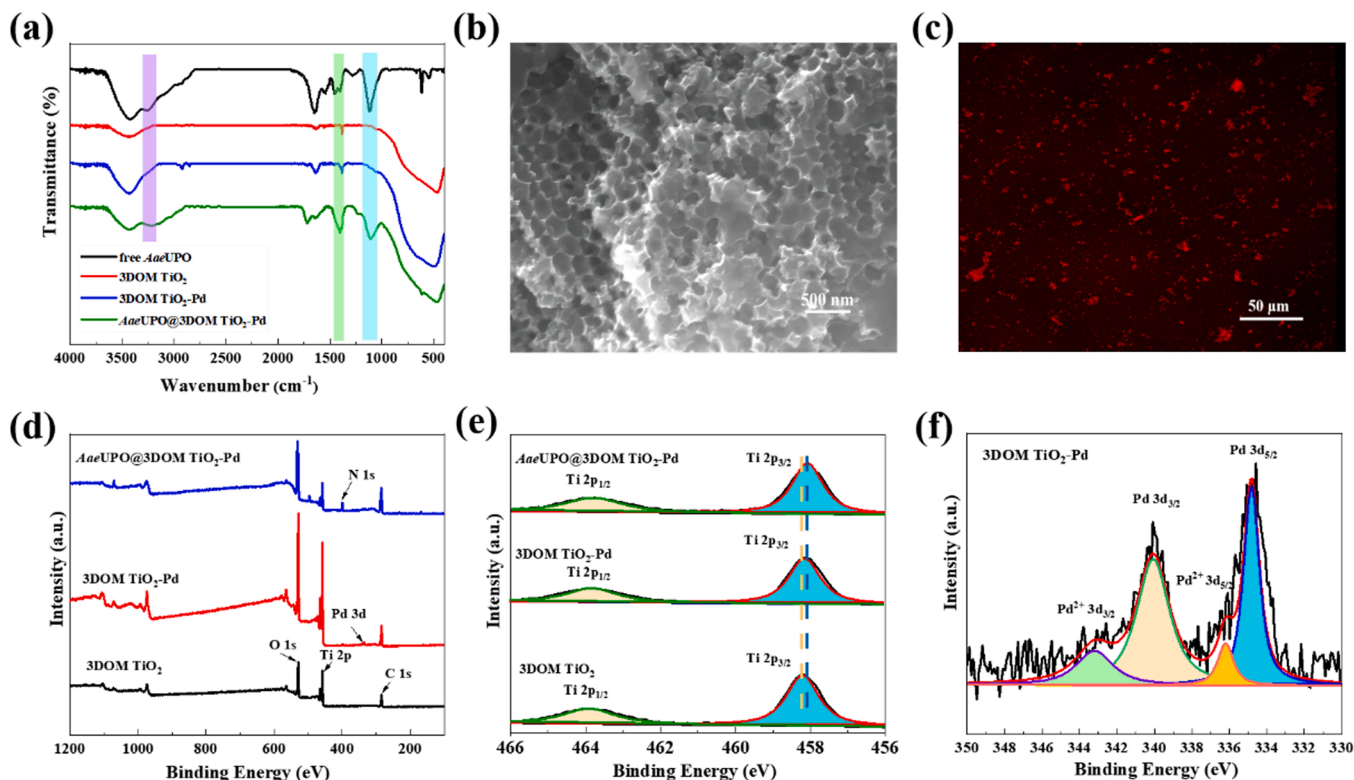


Fig. 4. FTIR spectra (a) of free AaeUPO , 3DOM TiO_2 , 3DOM $\text{TiO}_2\text{-Pd}$ and $\text{AaeUPO}@3\text{DOM TiO}_2\text{-Pd}$; SEM image (b) and CLSM image (c) of $\text{AaeUPO}@3\text{DOM TiO}_2\text{-Pd}$; XPS spectra (d) and Ti 2p spectra (e) of 3DOM TiO_2 , 3DOM $\text{TiO}_2\text{-Pd}$ and $\text{AaeUPO}@3\text{DOM TiO}_2\text{-Pd}$; Pd 3d spectrum (f) of 3DOM $\text{TiO}_2\text{-Pd}$.

3.2. Optimization of immobilization conditions for AaeUPO@3DOM TiO₂-Pd

After AaeUPO was precipitated by saturated ammonium sulfate, the immobilized enzyme was prepared by cross-linking AaeUPO with different concentrations of GA. As shown in Fig. 5a, when GA was not added, free AaeUPO was mainly immobilized on the carrier in the state of single enzyme molecule by physical adsorption. In cases like that, the binding force of the enzyme to carrier was not strong, and the amount of immobilized enzyme was small. With the increase of GA concentration, the relative activity of AaeUPO@3DOM TiO₂-Pd first increased and then decreased. The relative enzyme activity reached the maximum at GA concentration of 0.25 %, 9 times that without GA indicating the superiority of immobilizing CLEAs. When a lower GA concentration was used, a considerable number of enzyme molecules in the macropores were not successfully cross-linked thus easily leaking and inducing the lower activity recovery. The high concentration of GA will change the conformation of enzyme molecules and reduce the relative activity of immobilized enzyme [53,54]. The effect of crosslinking time on the preparation of AaeUPO@3DOM TiO₂-Pd is shown in Fig. 5b. The relative enzyme activity of AaeUPO@3DOM TiO₂-Pd was the highest at cross-linking time of 40 min. With short cross-linking time, the cross-linking of the enzyme molecules in macropores would be insufficient. With too long cross-linking time, the CLEAs formed in the macropores would be too dense causing the overlap of active sites of the enzyme molecules and affecting the contact between active sites and the substrate. Finally, the GA concentration of 0.25 % and the cross-linking time of 40 min were used for subsequent experiments.

BSA was added to reduce the negative effect of high reactive GA on the amino acid residues on enzyme molecule surface. Fig. 5c shows the effect of BSA:AaeUPO ratios on the enzyme activity of AaeUPO@3DOM TiO₂-Pd. At BSA:AaeUPO ratio of 2:1, the relative enzyme activity of AaeUPO@3DOM TiO₂-Pd was the highest, which was 1.56 times that without BSA protective agent. As an amino acid donor, BSA can provide enough amino acid residues to counteract the high reactivity of GA to enzyme molecules during the cross-linking process. The low relative enzyme activity of AaeUPO@3DOM TiO₂-Pd at low ratio of BSA and AaeUPO was due to the lack of sufficient lysine in the solution to participate in the Schiff base reaction. In contrast, when the amount of BSA was too high, the surface residues of BSA will compete with AaeUPO for GA molecules, making it difficult for AaeUPO to cross-link sufficiently. On the other hand, the steric hindrance formed by excess BSA would hinder the AaeUPO active sites from contacting the substrate, resulting in a decrease in the apparent activity of AaeUPO@3DOM TiO₂-Pd. The ratio of BSA to AaeUPO used in the final experiment was 2:1.

Fig. 5d shows the effect of buffer pH on the activity of AaeUPO@3DOM TiO₂-Pd during immobilization. The relative activity of AaeUPO@3DOM TiO₂-Pd was the highest at pH = 3.0. Probably because during the immobilization process, when the pH of buffer solution was 3.0, the enzyme molecules were most easily precipitated from the solution thus providing enough enzyme molecules for subsequent cross-linking reaction. Finally, AaeUPO@3DOM TiO₂-Pd was prepared with GA concentration of 0.25 %, crosslinking time of 40 min, 2:1 ratio of BSA and AaeUPO, and pH = 3.0 as the immobilization conditions.

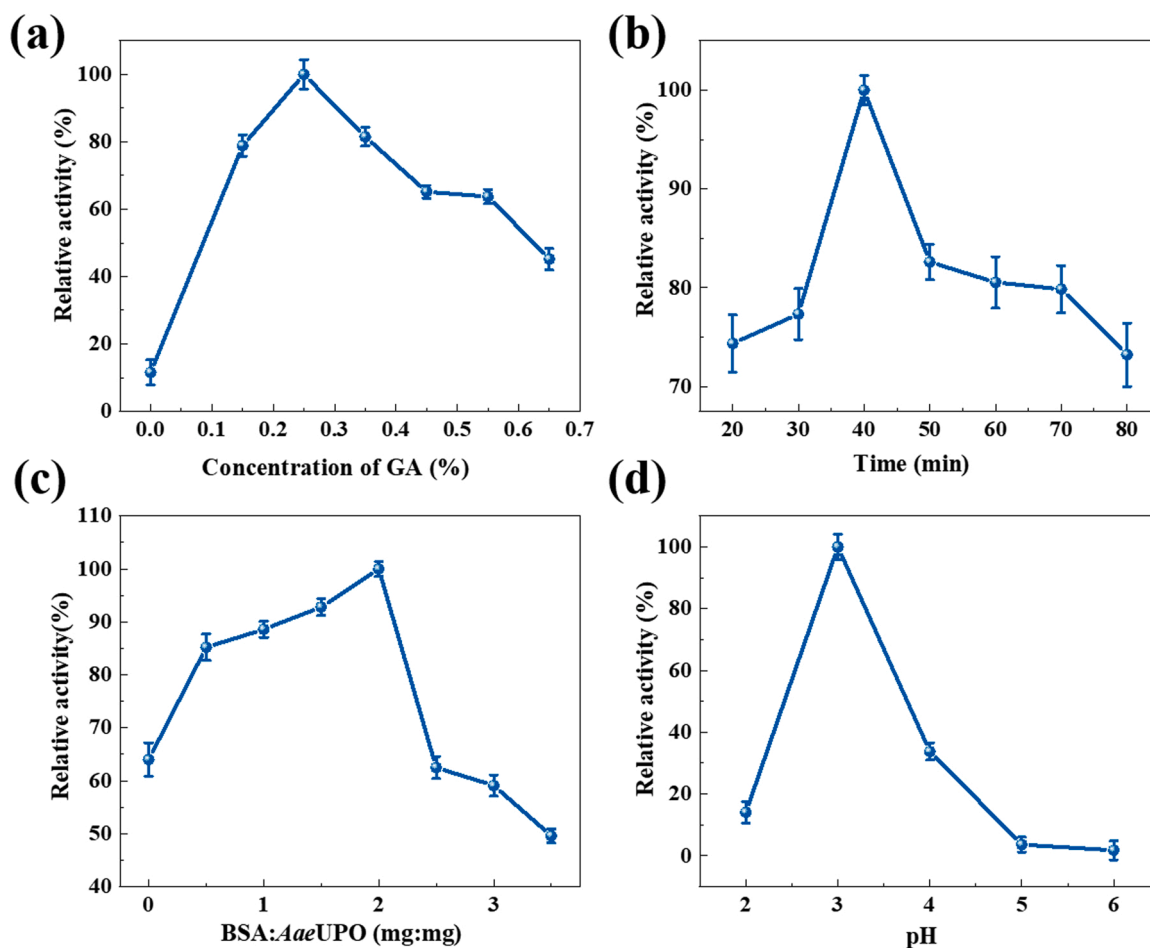


Fig. 5. Optimization of immobilization conditions for the preparation of AaeUPO@3DOM TiO₂-Pd: GA content (a), cross-linking time (b), BSA and AaeUPO ratio (c), pH (d).

3.3. Effect of reaction conditions on AaeUPO activity

The effect of reaction pH on the activity of AaeUPO was investigated, and CLEAs-AaeUPO was prepared as a control. As shown in Fig. 6a, The optimum pH of free enzyme was 5, while the optimum pH of AaeUPO@3DOM TiO₂-Pd and CLEAs-AaeUPO were both 6. The change of optimal reaction pH of AaeUPO@3DOM TiO₂-Pd to neutral may be attributed to transformation of the enzyme molecule structure as well as surface charges during the crosslinking. In the process of crosslinking, the crosslinker may cross-link the amino group on the surface of the enzyme molecule, resulting in negative charge of the acid group on the surface, which makes the reaction conditions milder.

As shown in Fig. 6b, the effects of temperature on the enzyme activity of free AaeUPO, CLEAs-AaeUPO and AaeUPO@3DOM TiO₂-Pd were determined in the range of 10–70 °C. The optimum catalytic temperature of the free enzyme was 30 °C. After immobilization, the optimal catalytic temperature of CLEAs-AaeUPO and AaeUPO@3DOM TiO₂-Pd was increased to 40 °C. The reason was that after cross-linking, the multi-site covalent interaction between the enzyme molecules improved the rigidity of the enzyme molecules, making the enzyme structure less sensitive to heat. Under the optimal conditions, the activity of AaeUPO@3DOM TiO₂-Pd was 151 U/g_{carrier} (Eq. (S2)), and the recovery of enzyme activity (Eq. (S3)) was 30 %, which was higher than that of CLEAs (12 %).

3.4. Kinetic studies

We compared the kinetic properties of free enzyme, CLEAs-AaeUPO and AaeUPO@3DOM TiO₂-Pd. As shown in Table 1 and Fig. S5, the V_{\max} value of AaeUPO@3DOM TiO₂-Pd (1.741 mM/min) was higher than that of CLEAs-AaeUPO (1.105 mM/min). Both were lower than free AaeUPO (2.896 mM/min). The increased reaction rate of AaeUPO@3DOM TiO₂-Pd may be because the support structure in AaeUPO@3DOM TiO₂-Pd made the formed CLEAs less prone to agglomeration compared with CLEAs-AaeUPO, which enhanced substrate accessibility [51]. The V_{\max} of free enzyme was higher than that of immobilized enzyme. This indicated that the conformational freedom of AaeUPO and the contact of the active site and substrate were reduced after cross-linking. The K_m value of AaeUPO@3DOM TiO₂-Pd (13.469 mM) was lower than that of CLEAs-AaeUPO (16.033 mM), and the K_m value of free enzyme (7.061 mM) was the lowest. These results suggested that the CLEAs formed after cross-linking affected the permeation rates of substrates and products. AaeUPO@3DOM TiO₂-Pd had higher substrate affinity than CLEAs-AaeUPO because of the compartments connected by porous channels leading to better accessibility to substrates. In addition, the ordered macroporous structure effectively prevented the agglomeration

Table 1

Kinetic parameters of free AaeUPO, CLEAs-AaeUPO, AaeUPO@3DOM TiO₂-Pd.

Biocatalyst	V_{\max} (mM/min)	K_m (mM)
Free AaeUPO	2.896	7.061
CLEAs-AaeUPO	1.105	16.033
AaeUPO@3DOM TiO ₂ -Pd	1.741	13.439

of CLEAs particles and reduced the particle size of CLEAs, thereby improving the mass transfer and diffusion of the substrates and products. The construction of AaeUPO@3DOM TiO₂-Pd successfully solved the issues of low reaction rate and poor substrate affinity of CLEAs-AaeUPO.

3.5. Study of stability

The stability of free enzyme, CLEAs-AaeUPO, and AaeUPO@3DOM TiO₂-Pd immersed in buffer solutions at pH 3.0 and 9.0 was investigated, and the relative activities at the optimal pH conditions were determined. As shown in Fig. 7a, after incubation at pH 3.0 and 9.0 for 6 h, AaeUPO@3DOM TiO₂-Pd retained more than 84.0 % and 87.0 % of the original activities, respectively, which was higher than CLEAs-AaeUPO let alone free AaeUPO under the same conditions. The improved stability of AaeUPO@3DOM TiO₂-Pd under harsh pH conditions was because that AaeUPO@3DOM TiO₂-Pd provided a relatively stable microenvironment to prevent the dissociation of subunits of CLEAs. Besides, the confinement of the macropores of the AaeUPO@3DOM TiO₂-Pd inhibited the unfolding-refolding movement of the enzymatic protein for denaturation, thereby preserving its activity. Therefore the thermal stability can also be enhanced. Fig. 7b showed the inactivation rate of free enzyme and CLEAs-AaeUPO was faster than that of AaeUPO@3DOM TiO₂-Pd at 50 °C. After 6 h of incubation, free AaeUPO retained only 37.9 % of its initial activity, while 75.3 % for CLEAs-AaeUPO and 89.0 % for AaeUPO@3DOM TiO₂-Pd.

In industrial applications, severe vibration was effective to decrease mass transfer limitations. Therefore, the mechanical stability of enzymes was determined by shaking conditions (200 r/min). As shown in Fig. 7c, in aqueous solution, free enzyme activity dropped sharply to 0 within 4 days. The activity of CLEAs-AaeUPO decreased slowly and retained about 30 % of the initial enzyme activity after 12 days. The slow decrease in the activity of CLEAs-AaeUPO may be due to the fact that CLEAs-AaeUPO became relatively compact under shaking conditions, and the active site was encapsulated. On the one hand, this resulted in a decrease in the relative activity of CLEAs-AaeUPO. On the other hand, the relatively compact structure would also protect the active site of AaeUPO to some extent. AaeUPO@3DOM TiO₂-Pd can further maintain more than 80 % of the initial activity after shaking for 12 days. Because

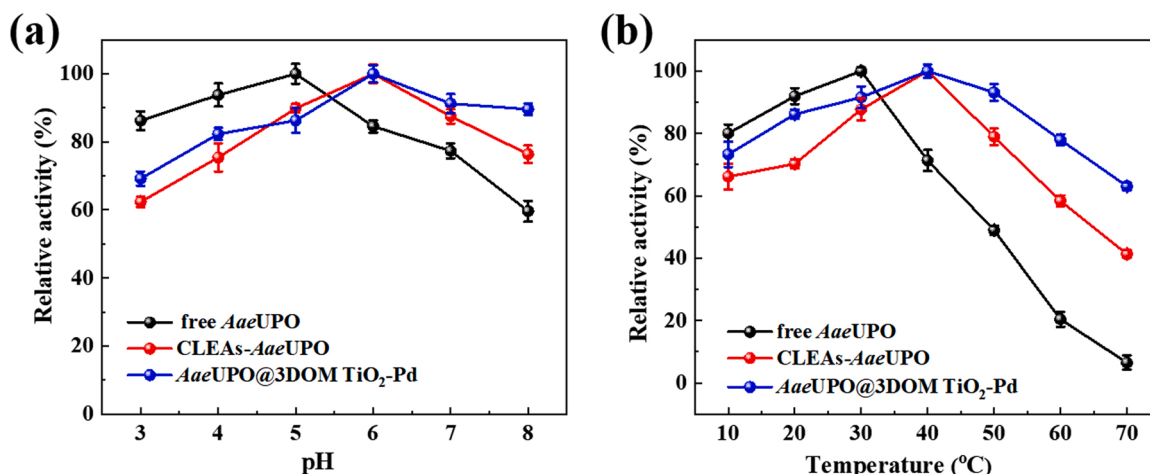


Fig. 6. Effect of reaction pH (a) and temperature (b) on enzyme activity.

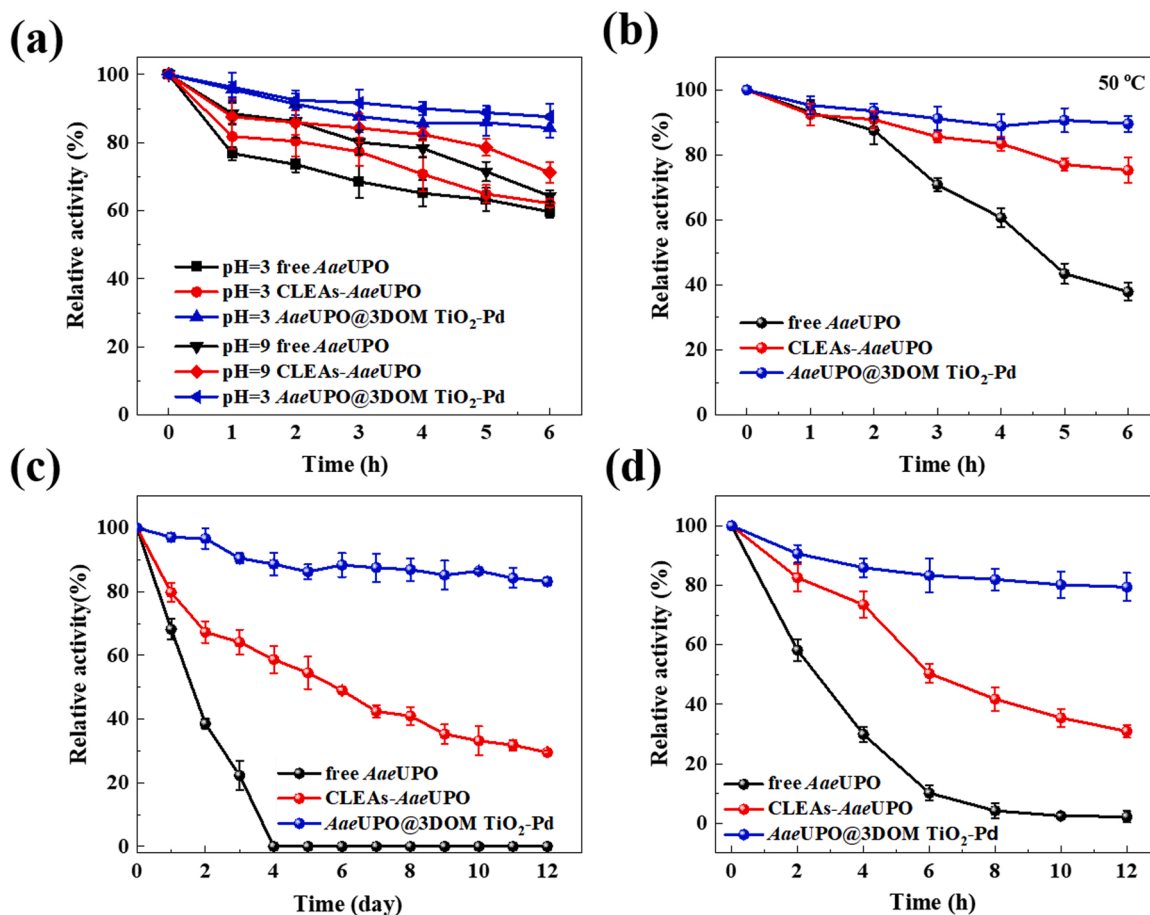


Fig. 7. pH (a), thermal (b), mechanical (c) and light stabilities (d) of the free *AaeUPO*, *CLEAs-AaeUPO* and *AaeUPO@3DOM TiO₂-Pd*.

the macropore skeleton of 3DOM $\text{TiO}_2\text{-Pd}$ decreased the influence of external shear force on enzyme molecules. As shown in Fig. S6, the overall morphology of *AaeUPO@3DOM TiO₂-Pd* did not noticeably change after mechanical stability test. Therefore, this method of *CLEAs* encapsulated in 3DOM structure may have great application potential in the biocatalysis industry.

Fig. 7d shows the influence of light irradiation on the activities of free enzyme, *CLEAs-AaeUPO*, and *AaeUPO@3DOM TiO₂-Pd*. The activity of free enzyme decreased sharply under light with only 10 % of the initial activity retained after 6 h, and almost no activity was retained after 12 h. After 12 h of continuous light irradiation, the *CLEAs* could retain 30 % of the initial activity. The activity of *AaeUPO@3DOM TiO₂-Pd* decreased the most slowly with about 80 % retained after 12 h. The energy released by simulated sunlight led to changes in the spatial structure of the enzyme, resulting in the loss of activity of free enzyme and *CLEAs-AaeUPO*. The macroporous skeleton of 3DOM $\text{TiO}_2\text{-Pd}$ could effectively shield the damage of direct light irradiation on the active sites of *AaeUPO*. And the confinement of pores could also limit the conformational change of *CLEAs*, protecting the active site of the enzyme.

3.6. (*R*)-1-phenylethanol production

As schemed in Fig. 8a, the enantio- and stereoselective hydroxylation of ethylbenzene into (*R*)-1-phenylethanol was used as model reaction to validate the photo-enzyme-coupled catalysis by the obtained *AaeUPO@3DOM TiO₂-Pd* under simulated sunlight. The conversion of ethylbenzene increased with the increase of pH (Fig. 8b). The conversion rate of ethylbenzene reached its highest at pH= 6.0. The pH value affects the catalytic effect by changing the ionic state of enzyme surface and the

microenvironment of enzyme active center, therefore a proper pH can endow the enzyme with relatively high performance.

As shown in Fig. 8c, with the addition of methanol, the conversion rate of ethylbenzene increased rapidly and reached the highest at the methanol concentration of 32 mM. With further increasing the methanol concentration, the ethylbenzene conversion began to decrease. Under simulated sunlight, the participation of water in the oxidation process will generate reactive oxygen species (ROS), which will reduce the stability of *AaeUPO*. After adding methanol, the oxidation rate of methanol is faster than water, and the oxidation of methanol instead of water can not only accelerate the generation of H_2O_2 , but also prevent the formation of ROS during water oxidation thus reducing the negative effect of ROS. The $\bullet\text{OH}$ produced in the process of photoreaction can inactivate enzymes[55]. The influence of $\bullet\text{OH}$ on the catalyst was eliminated by adding methanol (Fig. S7), and the stability of catalyst was improved (Fig. 7d). However, at excess concentration, methanol as alcohol affects the active sites of *AaeUPO* and decreases the catalysis performance of *AaeUPO@3DOM TiO₂-Pd*.

After increasing the dosage of *AaeUPO@3DOM TiO₂-Pd* (Fig. 8d), the ethylbenzene conversion increased attributed to the increase of photocatalyst and enzyme catalyst. And then the ethylbenzene conversion almost kept steady, because the catalyst amount is no longer the rate-determining step. Continuing to increase the dosage of catalyst will only increase the reaction cost with neglected improvement of the conversion rate.

The conversion rate of ethylbenzene after immobilization in different photocatalysts was compared (Fig. S8). When the amount of Pd was 0.5 %, the conversion of ethylbenzene was the highest, which was consistent with the H_2O_2 production curve (Fig. 3c). As shown in Fig. 8e, the conversion of ethylbenzene by free enzyme (38 %) and *CLEAs-AaeUPO*

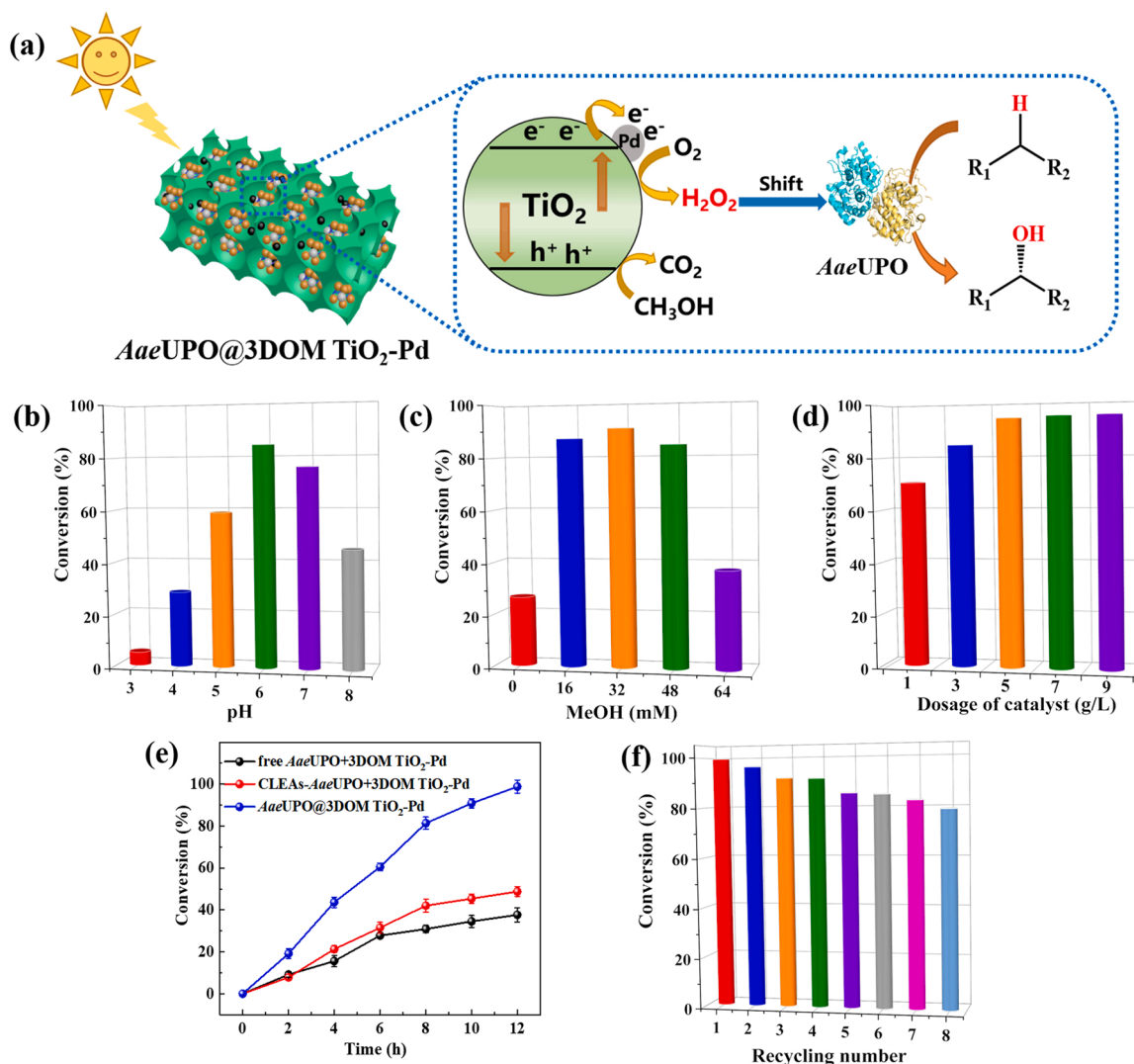


Fig. 8. Photoenzymatic hydroxylation by AaeUPO@3DOM TiO₂-Pd (a); the influence of pH (b), MeOH content (c), and dosage of catalyst (d) on ethylbenzene conversion rate; comparison of ethylbenzene conversion rate catalyzed by free AaeUPO, CLEAs-AaeUPO, and AaeUPO@3DOM TiO₂-Pd (e); reusability of AaeUPO@3DOM TiO₂-Pd (f).

(49 %) after adding H₂O₂ was very low, while that of AaeUPO@3DOM TiO₂-Pd with in situ photocatalytic H₂O₂ production was much higher (99 %) with enantiomeric excess (ee) value of > 99 %. The reason was that AaeUPO@3DOM TiO₂-Pd provided a monodisperse state for CLEAs-AaeUPO thus facilitating the contact of substrate and enzyme. We studied the effect of additional H₂O₂ on enzyme activity (Fig. S9). Because adding H₂O₂ could destroy the active site of AaeUPO, less than 12 % of original activity of AaeUPO was retained for free enzyme and AaeUPO@3DOM TiO₂-Pd after adding H₂O₂ for 3 h. The photocatalytic process provides H₂O₂ as substrate for AaeUPO catalysis to realize the cascade reaction, which benefits from the structure of the integrated catalyst. H₂O₂ produced in situ by photocatalysis is quickly transferred to the active center of enzyme thus accelerating reaction speed. The proximity effect of the two catalysts can reduce mass transfer resistance and provide better synergistic effect for the cascade reaction. Furthermore, H₂O₂ generated by photocatalysis is directly and quickly utilized by enzymes to avoid its accumulation, thus avoiding the severe damage to enzymes (Fig. S9) [33,56]. Enzyme stability was enhanced due to the protection of macropores to maintain a high activity during the reaction. The reusability of AaeUPO@3DOM TiO₂-Pd was shown in Fig. 8f. After recycling 8 times, AaeUPO@3DOM TiO₂-Pd still had 80 % conversion indicating excellent reusability attributed to the protection of

macropores and the in situ production of H₂O₂. The catalytic ability of the integrated catalyst decreased during repeated use, which was attributed to the damage of enzyme caused by the active oxygen generated by the photocatalytic part. In order to analyze the structural stability, the AaeUPO@3DOM TiO₂-Pd was characterized by SEM measurements after repeated use 8 times. As shown in Fig. S10, the morphology and macropore structure of AaeUPO@3DOM TiO₂-Pd have not been damaged, indicating that AaeUPO@3DOM TiO₂-Pd has good structural stability.

To further demonstrate the advantages of integrated catalyst in application, we added two or three equivalent enzymes to the reaction system (Fig. S11). It turns out that more enzymes did speed up the reaction, while the time to fulfill the whole conversion is similar. Although it saves the complicated preparation process of integrated catalyst, it has the inevitable problem of poor recovery [57,58]. In the long run, the total product quantity of integrated catalyst system by reusing several times is much higher than that with poor recovery (Fig. 8f) [30,59,60]. And the integrated catalyst can reduce mass transfer resistance between photocatalysis and enzyme catalysis. Moreover, the price of enzyme is relatively high, and it is a common method to reduce the production cost by trying to immobilize the enzyme on solid carrier to enhance the purpose of recovery. Furthermore, enzyme immobilization on solid

carrier suppresses the unfolding of tertiary structure which offered a more stable biocatalyst that has greater stability than other systems making it tolerant in different actual reaction conditions (Fig. 7). In order to clarify the different effects of photocatalyst and enzyme catalyst. The integrated catalyst was deactivated and compared under dark and light conditions. The results showed (Fig. S12) that the target product could not be detected under dark conditions. And only under light, the H_2O_2 can be produced to supply for active enzyme molecules to ensure the reaction operation.

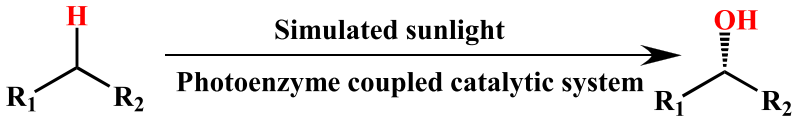
We studied the hydroxylation mechanism of AaeUPO with ethylbenzene as the substrate (Fig. S13). The heme iron in the catalytic active center of AaeUPO can combine with H_2O_2 to form Cpd-I, and then through electron rearrangement obtain Cpd-II. Cpd-II extracts a hydrogen atom from ethylbenzene to form Cpd-III. Finally, the active site of ethyl benzene binds to the hydroxyl group to produce phenyl ethanol. We use molecular simulations to study its chiral selectivity. Molecular simulation results (Fig. S14) showed that there was a conical channel above the active center of AaeUPO. There are aromatic residues

such as phenylalanine around the channel. The channel shape and polar residues can not only guide the hydrophobic substance to the active center, but also limit the rotation of phenyl substrate in the channel thus resulting in the formation of R-configuration phenyl ethanol.

Finally, we evaluated the substrate range of the reactions catalyzed by the photo-enzyme-coupled catalytic system. As shown in Table 2, a series of aromatic alkanes were effectively oxidized to the corresponding chiral alcohols with high selectivity and *ee* value (correlation equation in Supplementary material Eq. (S4–6)). Here we consider the volatilization of the substrate (Table S1). These chiral alcohols can be used as important intermediates to synthesize chiral drugs and natural products. Both methyl substitution and halogen substitution show high reactivity. The methyl group might be oxidized, but the content was very low (<0.3 %). We found that phenyl ethanol can be over-oxidized into ketones during the reaction process. However, we observed only a small amount of ketone production (no more than 1 %), which has little effect on the overall selectivity of this model reaction.

Table 2

Enantio- and stereoselective benzyl hydroxylation catalyzed by AaeUPO@3DOM TiO_2 -Pd under simulated sunlight.^a

					
Entry	Substrate	Product	Selectivity (%)	GC yield (%)	<i>ee</i> (%) ^c
1 ^b			> 99	98	> 99
2 ^b			> 99	85	> 93
3 ^b			> 99	70	> 97
4 ^b			> 98	69	> 87
5 ^b			> 99	94	> 92
6 ^b			99	92	> 95
7 ^b			> 99	90	> 94
8 ^b			> 99	86	> 89
9 ^b			> 99	82	> 94

a Reaction conditions: AaeUPO@3DOM TiO_2 -Pd (5 mg/mL), pH= 6.0, the light source is 300 W xenon lamp, reaction time = 12 h, T = 25 °C.

b Initial substrate concentration= 15 mM. c *ee* (%), detailed calculation procedure in supplementary material Eq. S6.

4. Conclusion

In conclusion, photocatalyst-based carrier was synthesized to immobilize UPOs to in situ generate H_2O_2 for photo-enzyme-coupled catalysis. To be specific, PS microspheres with ordered structure were used as template to obtain 3DOM TiO_2 with ordered macropores, followed by Pd loading with good dispersion. The loading of Pd extended the range of light response and improved the spatial separation of photogenerated electrons and holes. H_2O_2 production could increase to 18.9 times after optimum Pd loading. Then AaeUPO was successfully immobilized in the macroporous channels of the 3DOM TiO_2 -Pd photocatalyst in the form of CLEAs using GA as cross-linking agent and BSA as protective protein. Compared with CLEAs-AaeUPO, the construction of AaeUPO@3DOM TiO_2 -Pd achieved monodisperse CLEAs, and improved the mass transfer of the substrate and product thus solving the issues of poor substrate accessibility of CLEAs-AaeUPO. Besides, photo-enzyme-coupled catalytic system could generate H_2O_2 in situ thus reducing the diffusion distance to enzyme. AaeUPO@3DOM TiO_2 -Pd exhibited stronger acid-base tolerance, thermostability, mechanical stability and light stability compared with CLEAs-AaeUPO and free enzyme attributed to the protection of macropores of the AaeUPO@3DOM TiO_2 -Pd and the in situ generated H_2O_2 . When AaeUPO@3DOM TiO_2 -Pd was used for the enantio- and stereoselective hydroxylation of ethylbenzene to (R)-1-phenylethanol, under simulated sunlight conditions for in situ photocatalytic H_2O_2 production, the conversion rate reached 99 % with *ee* value of > 99 %, while the conversion rates of free enzyme and CLEAs-AaeUPO by adding H_2O_2 were only 38 % and 49 %, respectively. The AaeUPO@3DOM TiO_2 -Pd could be recycled up to 8 times and showed good reactivity towards other aromatic alkanes substrates. The encapsulation of CLEAs in metal-loaded 3DOM photocatalyst could be used for various photo-enzyme integrated catalysis, especially for the application prospect of UPO for selective oxyfunctionalization of C-H and C=C bonds. The prepared integrated catalyst has outstanding advantages in protecting and recycling AaeUPO. Although there is still a distance between this and the specific application, its industrial application potential is huge.

CRediT authorship contribution statement

Xuewu Deng: Conceptualization, Methodology, Writing – original draft, Visualization. **Xiaobing Zheng:** Conceptualization, Methodology, Formal analysis, Writing – original draft. **Feifei Jia:** Data curation. **Cuiyao Cao:** Data curation. **Haolei Song:** Supervision. **Yanjuan Jiang:** Supervision, Project administration. **Yunting Liu:** Supervision, Project administration. **Guanhua Liu:** Conceptualization, Writing – review & editing, Supervision, Funding acquisition. **Shijie Li:** Conceptualization, Supervision, Project administration. **Lihui Wang:** Supervision, Funding acquisition.

Declaration of Competing Interest

The authors declare that they have no known competing financial interests or personal relationships that could have appeared to influence the work reported in this paper.

Data Availability

Data will be made available on request.

Acknowledgments

This work was financially supported by the National Key Research and Development Program of China (2021YFC2104100), the National Natural Science Foundation of China (22178083, 21908040, 21901058, 51708504 and 22078081), the Hebei Key Research and Development Project (21372805D, 21372804D and 20372802D), Science Technology

Research Project of Higher Education of Hebei Province (QN2021045), Tianjin Science and Technology Project (22KPHDR00340, 22KPHDR00260), and the Natural Science Foundation of Tianjin City (20JCYBJC00530).

Appendix A. Supporting information

Supplementary data associated with this article can be found in the online version at [doi:10.1016/j.apcatb.2023.122622](https://doi.org/10.1016/j.apcatb.2023.122622).

References

- [1] Z.C. Litman, Y. Wang, H. Zhao, J.F. Hartwig, Cooperative asymmetric reactions combining photocatalysis and enzymatic catalysis, *Nature* 560 (7718) (2018) 355–359, <https://doi.org/10.1038/s41586-018-0413-7>.
- [2] S.J. Freakeley, S. Kochius, J. van Marwijk, C. Fenner, R.J. Lewis, K. Baldenius, S. S. Marais, D.J. Opperman, S.T.L. Harrison, M. Alcalde, M.S. Smit, G.J. Hutchings, A chemo-enzymatic oxidation cascade to activate C–H bonds with in situ generated H_2O_2 , *Nat. Commun.* 10 (1) (2019) 4178, <https://doi.org/10.1038/s41467-019-12120-w>.
- [3] M.M.C.H. van Schie, W. Zhang, F. Tieves, D.S. Choi, C.B. Park, B.O. Burek, J. Z. Bloh, I.W.C.E. Arends, C.E. Paul, M. Alcalde, F. Hollmann, Cascading g- C_3N_4 and peroxigenases for selective oxyfunctionalization reactions, *ACS Catal.* 9 (8) (2019) 7409–7417, <https://doi.org/10.1021/acscatal.9b01341>.
- [4] W. Zhang, B.O. Burek, E. Fernandez-Fueyo, M. Alcalde, J.Z. Bloh, F. Hollmann, Selective activation of C–H bonds in a cascade process combining photochemistry and biocatalysis, *Angew. Chem. Int. Ed. Engl.* 56 (48) (2017) 15451–15455, <https://doi.org/10.1002/anie.201708668>.
- [5] W. Zhang, H. Liu, M. van Schie, P.L. Hagedoorn, M. Alcalde, A.G. Denkova, K. Djanashvili, F. Hollmann, Nuclear waste and biocatalysis: a sustainable liaison, *ACS Catal.* 10 (23) (2020) 14195–14200, <https://doi.org/10.1021/acscatal.0c03059>.
- [6] P. De Santis, N. Petrovai, L.E. Meyer, M. Hobisch, S. Kara, A holistic carrier-bound immobilization approach for unspecific peroxxygenase, *Front. Chem.* 10 (2022), 985997, <https://doi.org/10.3389/fchem.2022.985997>.
- [7] B.O. Burek, S. Bormann, F. Hollmann, J.Z. Bloh, D. Holtmann, Hydrogen peroxide driven biocatalysis, *Green Chem.* 21 (12) (2019) 3232–3249, <https://doi.org/10.1039/C9GC00633H>.
- [8] S.J. Freakeley, S. Kochius, J. van Marwijk, C. Fenner, R.J. Lewis, K. Baldenius, S. S. Marais, D.J. Opperman, S.T.L. Harrison, M. Alcalde, M.S. Smit, G.J. Hutchings, A chemo-enzymatic oxidation cascade to activate C–H bonds with in situ generated H_2O_2 , *Nat. Commun.* 10 (1) (2019) 4178, <https://doi.org/10.1038/s41467-019-12120-w>.
- [9] H.L. Wapshott-Stehli, A.M. Grunden, In situ H_2O_2 generation methods in the context of enzyme biocatalysis, *Enzym. Microb. Tech.* 145 (2021), 109744, <https://doi.org/10.1016/j.enzmtech.2021.109744>.
- [10] Q. Hu, J. Yang, Z. Zheng, Y. Ding, Y. Chen, W. Gao, In situ H_2O_2 generation with gold nanoflowers as the coreactant accelerator for enzyme-free electrochemiluminescent immunosensing, *Biosens. Bioelectron.* 143 (2019), 111627, <https://doi.org/10.1016/j.bios.2019.111627>.
- [11] S. Li, C. Wang, Y. Liu, Y. Liu, M. Cai, W. Zhao, X. Du, S-Scheme MIL-101(Fe) octahedrons modified Bi_2WO_6 microspheres for photocatalytic decontamination of Cr(VI) and tetracycline hydrochloride: Synergistic insights, reaction pathways, and toxicity analysis, *Chem. Eng. J.* 455 (2023) 140943, <https://doi.org/10.1016/j.cej.2022.140943>.
- [12] X. Li, T. Liu, Y. Zhang, J. Cai, M. He, M. Li, Z. Chen, L. Zhang, Growth of BiOBr/ZIF-67 nanocomposites on carbon fiber cloth as filter-membrane-shaped photocatalyst for degrading pollutants in flowing wastewater, *Adv. Fiber Mater.* 4 (6) (2022) 1620–1631, <https://doi.org/10.1007/s42765-022-00189-w>.
- [13] C. Wang, R. Yan, M. Cai, Y. Liu, S. Li, A novel organic/inorganic S-scheme heterostructure of TCPP/ $\text{Bi}_{12}\text{O}_{17}\text{Cl}_2$ for boosting photodegradation of tetracycline hydrochloride: Kinetic, degradation mechanism, and toxic assessment, *Appl. Surf. Sci.* 610 (2023) 155346, <https://doi.org/10.1016/j.apsusc.2022.155346>.
- [14] X. Du, X. Yi, P. Wang, J. Deng, C. Wang, Enhanced photocatalytic Cr(VI) reduction and diclofenac sodium degradation under simulated sunlight irradiation over MIL-100(Fe)/g- C_3N_4 heterojunctions, *Chin. J. Catal.* 40 (1) (2019) 70–79, [https://doi.org/10.1016/S1872-2067\(18\)63160-2](https://doi.org/10.1016/S1872-2067(18)63160-2).
- [15] S. Li, M. Cai, Y. Liu, C. Wang, K. Lv, X. Chen, S-Scheme photocatalyst TaON/ Bi_2WO_6 nanofibers with oxygen vacancies for efficient abatement of antibiotics and Cr(VI): Intermediate eco-toxicity analysis and mechanistic insights, *Chin. J. Catal.* 43 (10) (2022) 2652–2664, [https://doi.org/10.1016/S1872-2067\(22\)64106-8](https://doi.org/10.1016/S1872-2067(22)64106-8).
- [16] S. Li, M. Cai, Y. Liu, C. Wang, R. Yan, X. Chen, Constructing $\text{Cd}_{0.5}\text{Zn}_{0.5}\text{S}/\text{Bi}_2\text{WO}_6$ S-scheme heterojunction for boosted photocatalytic antibiotic oxidation and Cr(VI) reduction, *Adv. Powder Mater.* 2 (1) (2023), 100073, <https://doi.org/10.1016/j.apmat.2022.100073>.
- [17] Y. Gao, X. Niu, Y. Qin, T. Guo, Y. Ji, G. Li, T. An, Unexpected culprit of increased estrogenic effects: Oligomers in the photodegradation of preservative ethylparaben in water, *Water Res.* 176 (2020), 115745, <https://doi.org/10.1016/j.watres.2020.115745>.
- [18] T. An, H. Yang, G. Li, W. Song, W.J. Cooper, X. Nie, Kinetics and mechanism of advanced oxidation processes (AOPs) in degradation of ciprofloxacin in water,

- Appl. Catal. B 94 (3) (2010) 288–294, <https://doi.org/10.1016/j.apcatb.2009.12.002>.
- [19] P.-S. Wang, X.-H. Yi, X. Xu, H. Ji, A.M. Alanazi, C.-C. Wang, C. Zhao, Y.V. Kaneti, P. Wang, W. Liu, Y. Yamauchi, Eliminating tetracycline antibiotics matrix via photoactivated sulfate radical-based advanced oxidation process over the immobilized MIL-88A: Batch and continuous experiments, Chem. Eng. J. 431 (2022), 133213, <https://doi.org/10.1016/j.cej.2021.133213>.
- [20] T. An, J. An, Y. Gao, G. Li, H. Fang, W. Song, Photocatalytic degradation and mineralization mechanism and toxicity assessment of antiviral drug acyclovir: experimental and theoretical studies, Appl. Catal. B 164 (2015) 279–287, <https://doi.org/10.1016/j.apcatb.2014.09.009>.
- [21] S. Li, M. Cai, C. Wang, Y. Liu, Ta₃N₅/CdS core-shell S-scheme heterojunction nanofibers for efficient photocatalytic removal of antibiotic tetracycline and Cr (VI): performance and mechanism insights, Adv. Fiber Mater. (2023), <https://doi.org/10.1007/s42765-022-00253-5>.
- [22] W. Wang, H. Xie, G. Li, J. Li, P.K. Wong, T. An, Visible light-induced marine bacterial inactivation in seawater by an in situ photo-fenton system without additional oxidants: implications for ballast water sterilization, ACS ES&T Water 1 (6) (2021) 1483–1494, <https://doi.org/10.1021/acsestwater.1c00048>.
- [23] W. Wang, W. Gu, G. Li, H. Xie, P.K. Wong, T. An, Few-layered tungsten selenide as a co-catalyst for visible-light-driven photocatalytic production of hydrogen peroxide for bacterial inactivation, Environ. Sci. Nano 7 (12) (2020) 3877–3887, <https://doi.org/10.1039/D0EN00801J>.
- [24] S. Zhang, S. Liu, Y. Sun, S. Li, J. Shi, Z. Jiang, Enzyme-photo-coupled catalytic systems, Chem. Soc. Rev. 50 (24) (2021) 13449–13466, <https://doi.org/10.1039/D1CS00392E>.
- [25] J. Kim, T.V.T. Nguyen, Y.H. Kim, F. Hollmann, C.B. Park, Lignin as a multifunctional photocatalyst for solar-powered biocatalytic oxofunctionalization of C–H bonds, Nat. Synth. 1 (3) (2022) 217–226, <https://doi.org/10.1038/s44160-022-00035-2>.
- [26] K.P. Sokol, W.E. Robinson, J. Warnan, N. Kornienko, M.M. Nowaczyk, A. Ruff, J. Z. Zhang, E. Reisner, Bias-free photoelectrochemical water splitting with photosystem II on a dye-sensitized photoanode wired to hydrogenase, Nat. Energy 3 (11) (2018) 944–951, <https://doi.org/10.1038/s41560-018-0232-y>.
- [27] J.Z. Zhang, E. Reisner, Advancing photosystem II photoelectrochemistry for semi-artificial photosynthesis, Nat. Rev. Chem. 4 (1) (2020) 6–21, <https://doi.org/10.1038/s41570-019-0149-4>.
- [28] T.E. Miller, T. Beneyton, T. Schwander, C. Diehl, M. Girault, R. McLean, T. Chotel, P. Claus, N.S. Cortina, J.-C. Baret, T.J. Erb, Light-powered CO₂ fixation in a chloroplast mimic with natural and synthetic parts, Science 368 (6491) (2020) 649–654, <https://doi.org/10.1126/science.aaz6802>.
- [29] J.M. Bolivar, J.M. Woodley, R. Fernandez-Lafuente, Is enzyme immobilization a mature discipline? Some critical considerations to capitalize on the benefits of immobilization, Chem. Soc. Rev. 51 (15) (2022) 6251–6290, <https://doi.org/10.1039/D2CS00083K>.
- [30] R.A. Sheldon, A. Basso, D. Brady, New frontiers in enzyme immobilisation: robust biocatalysts for a circular bio-based economy, Chem. Soc. Rev. 50 (10) (2021) 5850–5862, <https://doi.org/10.1039/D1CS00015B>.
- [31] H. Zhao, G. Liu, Y. Liu, X. Liu, H. Wang, H. Chen, J. Gao, Y. Jiang, Metal Nanoparticles@Covalent Organic Framework@Enzymes: a universal platform for fabricating a metal–enzyme integrated nanocatalyst, ACS Appl. Mater. Inter. 14 (2) (2022) 2881–2892, <https://doi.org/10.1021/acsami.1c21264>.
- [32] J. Brehm, R.J. Lewis, T. Richards, T. Qin, D.J. Morgan, T.E. Davies, L. Chen, X. Liu, G.J. Hutchings, Enhancing the chemo-enzymatic one-pot oxidation of cyclohexane via in situ H₂O₂ production over supported Pd-based catalysts, ACS Catal. (2022) 11776–11789, <https://doi.org/10.1021/acscatal.2c03051>.
- [33] J. Jia, Q. Huo, D. Yang, Y. Sun, S. Zhang, S. Li, J. Shi, Z. Jiang, Granum-inspired photoenzyme-coupled catalytic system via stacked polymeric carbon nitride, ACS Catal. 11 (15) (2021) 9210–9220, <https://doi.org/10.1021/acscatal.1c01555>.
- [34] J.D. Cui, L.L. Li, Y.M. Zhao, Simple technique for preparing stable and recyclable cross-linked enzyme aggregates with crude-pored microspherical silica core, Ind. Eng. Chem. Res. 53 (42) (2014) 16176–16182, <https://doi.org/10.1021/ie5021206>.
- [35] Y. Jiang, L. Shi, Y. Huang, J. Gao, X. Zhang, L. Zhou, Preparation of robust biocatalyst based on cross-linked enzyme aggregates entrapped in three-dimensionally ordered macroporous silica, ACS Appl. Mater. Interface 6 (4) (2014) 2622–2628, <https://doi.org/10.1021/am405104b>.
- [36] Y. Jiang, P. Zheng, L. Zhou, W. Kong, J. Gao, J. Wang, J. Gu, X. Zhang, X. Wang, Immobilization of lipase in hierarchically ordered macroporous/mesoporous silica with improved catalytic performance, J. Mol. Catal. B-Enzym 130 (2016) 96–103, <https://doi.org/10.1016/j.molcatb.2016.05.009>.
- [37] X. Liu, G. Zhu, X. Wang, X. Yuan, T. Lin, F. Huang, Progress in black titania: a new material for advanced photocatalysis, Adv. Energy Mater. 6 (17) (2016), <https://doi.org/10.1002/aenm.201600452>.
- [38] Y. Wei, Q. Wu, J. Xiong, J. Liu, Z. Zhao, Fabrication of ultrafine Pd nanoparticles on 3D ordered macroporous TiO₂ for enhanced catalytic activity during diesel soot combustion, Chin. J. Catal. 39 (4) (2018) 606–612, [https://doi.org/10.1016/S1872-2067\(17\)62939-5](https://doi.org/10.1016/S1872-2067(17)62939-5).
- [39] G. Li, X. Nie, J. Chen, P.K. Wong, T. An, H. Yamashita, H. Zhao, Enhanced simultaneous PEC eradication of bacteria and antibiotics by facilely fabricated high-activity {001} facets TiO₂ mounted onto TiO₂ nanotubular photoanode, Water Res. 101 (2016) 597–605, <https://doi.org/10.1016/j.watres.2016.06.001>.
- [40] X. Yang, H. Sun, G. Li, T. An, W. Choi, Fouling of TiO₂ induced by natural organic matters during photocatalytic water treatment: Mechanisms and regeneration strategy, Appl. Catal. B 294 (2021), 120252, <https://doi.org/10.1016/j.apcatb.2021.120252>.
- [41] G. Li, X. Nie, Y. Gao, T. An, Can environmental pharmaceuticals be photocatalytically degraded and completely mineralized in water using g-C₃N₄/TiO₂ under visible light irradiation?—Implications of persistent toxic intermediates, Appl. Catal. B 180 (2016) 726–732, <https://doi.org/10.1016/j.apcatb.2015.07.014>.
- [42] Y. Fu, K. Zhang, Y. Zhang, Y. Cong, Q. Wang, Fabrication of visible-light-active MR/NH₂-MIL-125(Ti) homojunction with boosted photocatalytic performance, Chem. Eng. J. 412 (2021), 128722, <https://doi.org/10.1016/j.cej.2021.128722>.
- [43] G. Liu, Y. Huang, H. Lv, H. Wang, Y. Zeng, M. Yuan, Q. Meng, C. Wang, Confining single-atom Pd on g-C₃N₄ with carbon vacancies towards enhanced photocatalytic NO conversion, Appl. Catal. B 284 (2021), 119683, <https://doi.org/10.1016/j.apcatb.2020.119683>.
- [44] W. Jones, D.J. Martin, A. Caravaca, A.M. Beale, M. Bowker, T. Maschmeyer, G. Hartley, A. Masters, A comparison of photocatalytic reforming reactions of methanol and triethanolamine with Pd supported on titania and graphitic carbon nitride, Appl. Catal. B 240 (2019) 373–379, <https://doi.org/10.1016/j.apcatb.2017.01.042>.
- [45] J. Guo, D. Ma, F. Sun, G. Zhuang, Q. Wang, A.M. Al-Enizi, A. Nafady, S. Ma, Substituent engineering in g-C₃N₄/COF heterojunctions for rapid charge separation and high photo-redox activity, Sci. China Chem. 65 (9) (2022) 1704–1709, <https://doi.org/10.1007/s11426-022-1350-1>.
- [46] H. Ou, G. Li, W. Ren, B. Pan, G. Luo, Z. Hu, D. Wang, Y. Li, Atomically dispersed Au-assisted C–C coupling on red phosphorus for CO₂ photoreduction to C₂H₆, J. Am. Chem. Soc. 144 (48) (2022) 22075–22082, <https://doi.org/10.1021/jacs.2c09424>.
- [47] S. Zheng, H. Du, L. Yang, M. Tan, N. Li, Y. Fu, D. Hao, Q. Wang, PDINH bridged NH₂-UiO-66(Zr) Z-scheme heterojunction for promoted photocatalytic Cr(VI) reduction and antibacterial activity, J. Hazard. Mater. 447 (2023), 130849, <https://doi.org/10.1016/j.jhazmat.2023.130849>.
- [48] H. Ou, S. Ning, P. Zhu, S. Chen, A. Han, Q. Kang, Z. Hu, J. Ye, D. Wang, Y. Li, Carbon nitride photocatalysts with integrated oxidation and reduction atomic active centers for improved CO₂ conversion, Angew. Chem. Int. Ed. 134 (34) (2022) e202206579.
- [49] S. Zhang, J. Shi, Y. Sun, Y. Wu, Y. Zhang, Z. Cai, Y. Chen, C. You, P. Han, Z. Jiang, Artificial thylakoid for the coordinated photoenzymatic reduction of carbon dioxide, ACS Catal. 9 (5) (2019) 3913–3925, <https://doi.org/10.1021/acscatal.9b00255>.
- [50] R. Tu, S. Chen, W. Cao, S. Zhang, L. Li, T. Ji, J. Zhu, J. Li, X. Lu, The effect of H₂O₂ desorption on achieving improved selectivity for direct synthesis of H₂O₂ over TiO₂(B)/anatase supported Pd catalyst, Catal. Commun. 89 (2017) 69–72, <https://doi.org/10.1016/j.catcom.2016.10.024>.
- [51] K. Sellami, A. Couvert, N. Nasrallah, R. Maachi, N. Tandjaoui, M. Abouseoud, A. Amrane, Bio-based and cost effective method for phenolic compounds removal using cross-linked enzyme aggregates, J. Hazard. Mater. 403 (2021), 124021, <https://doi.org/10.1016/j.jhazmat.2020.124021>.
- [52] J.S. Hero, A.H. Morales, N.I. Perotti, C.M. Romero, M.A. Martinez, Improved development in magnetic Xyl-CLEAs technology for biotransformation of agro-industrial by-products through the use of a novel macromolecular cross-linker, React. Funct. Polym. 154 (2020), <https://doi.org/10.1016/j.reactfunctpolym.2020.104676>.
- [53] B. Wei, F. Liu, X. Liu, L. Cheng, Q. Yuan, H. Gao, H. Liang, Enhancing stability and by-product tolerance of beta-glucuronidase based on magnetic cross-linked enzyme aggregates, Colloid Surf. B 210 (2022), 112241, <https://doi.org/10.1016/j.colsurfb.2021.112241>.
- [54] S. Kannan, M. Marudhamuthu, Development of chitin cross-linked enzyme aggregates of L-methioninase for upgraded activity, permanence and application as efficient therapeutic formulations, Int. J. Biol. Macromol. 141 (2019) 218–231, <https://doi.org/10.1016/j.ijbiomac.2019.08.246>.
- [55] B.O. Burek, S.R. deBoer, F. Tieves, W. Zhang, M. vanSchie, S. Bormann, M. Alcalde, D. Holtmann, F. Hollmann, D.W. Bahnemann, J.Z. Bloh, Photoenzymatic hydroxylation of ethylbenzene catalyzed by specific peroxxygenase: origin of enzyme inactivation and the impact of light intensity and temperature, ChemCatChem 11 (13) (2019) 3093–3100, <https://doi.org/10.1002/cctc.201900610>.
- [56] Y. Sun, J. Shi, Z. Wang, H. Wang, S. Zhang, Y. Wu, H. Wang, S. Li, Z. Jiang, Thylakoid membrane-inspired capsules with fortified cofactor shuttling for enzyme-photocoupled catalysis, J. Am. Chem. Soc. 144 (9) (2022) 4168–4177, <https://doi.org/10.1021/jacs.1c12790>.
- [57] Y. Li, L. Wen, T. Tan, Y. Lv, Sequential Co-immobilization of enzymes in metal-organic frameworks for efficient biocatalytic conversion of adsorbed CO₂ to formate, Front. Bioeng. Biotechnol. 7 (2019), <https://doi.org/10.3389/fbioe.2019.00394>.
- [58] R. DiCosimo, J. McAuliffe, A.J. Poulou, G. Bohlmann, Industrial use of immobilized enzymes, Chem. Soc. Rev. 42 (15) (2013) 6437–6474, <https://doi.org/10.1039/C3CS35506C>.
- [59] X. Pei, Z. Luo, L. Qiao, Q. Xiao, P. Zhang, A. Wang, R.A. Sheldon, Putting precision and elegance in enzyme immobilisation with bio-orthogonal chemistry, Chem. Soc. Rev. 51 (16) (2022) 7281–7304, <https://doi.org/10.1039/D1CS01004B>.
- [60] U. Hanefeld, L. Gardossi, E. Magner, Understanding enzyme immobilisation, Chem. Soc. Rev. 38 (2) (2009) 453–468, <https://doi.org/10.1039/B711564B>.